



Oblique fault movement during the 2016 Mw 5.9 Zaduo earthquake: insights into regional tectonics of the Qiangtang block, Tibetan Plateau

Jiansheng Yu · Bin Zhao · Wenbin Xu · Dongzhen Wang · Kai Tan

Received: 15 February 2020 / Accepted: 22 May 2020

© Springer Nature B.V. 2020

Abstract The present east–west crustal extension of the Tibetan Plateau has been demonstrated through field investigations, satellite imagery, geodetic deformation, and earthquake focal mechanisms. Normal faulting earthquakes in the interior Tibetan Plateau are almost entirely

Electronic supplementary material The online version of this article (<https://doi.org/10.1007/s10950-020-09930-7>) contains supplementary material, which is available to authorized users.

J. Yu · B. Zhao · D. Wang · K. Tan
Key Laboratory of Earthquake Geodesy, Institute of Seismology,
China Earthquake Administration, Wuhan 430071, China

J. Yu
e-mail: Janson@cgps.ac.cn

D. Wang
e-mail: dzwang@cgps.ac.cn

K. Tan
e-mail: tankai@cgps.ac.cn

B. Zhao
Institute of Disaster Prevention, Yanjiao, Sanhe City 065201
Hebei Province, China
e-mail: zhaobin@cgps.ac.cn

W. Xu
Central South University School of Geosciences and Info Physics,
Changsha 410083, China
e-mail: wenbin.xu@csu.edu.cn

W. Xu
Key Laboratory of Metallogenic Prediction of Nonferrous Metals
and Geological Environment Monitoring, Central South
University, Changsha 410083, China

confined to regions at elevations over 4000 m. However, our knowledge of the eastward extent of normal faulting in the plateau is still uncertain due to the limited occurrence of well-documented earthquakes. Based on a retrospective analysis of the 2016 Mw 5.9 Zaduo earthquake in the Tibetan Plateau, we consider the NE trending Zaduo-Shanglaxiu fault as the most likely rupture fault through a comprehensive analysis of relocated aftershock sequences, mapped active faults, and newly acquired strain rate tensor. We further determine seismogenic fault geometry using a Bayesian approach and sample with a Markov Chain Monte Carlo method. We interpret the Zaduo earthquake to reflect the release of slowly accumulated elastic strain accumulated mainly by gravitational forces rather than a delay triggering event from the 2010 Yushu earthquake. The viscoelastic calculations to estimate Coulomb stress changes over time indicate that long-term viscous flow in a weak mid-crust can load adjacent faults far more than static stress changes alone. Our results show that the Zaduo earthquake was a Mw 5.9 oblique normal faulting event that occurred in the easternmost part of the Tibetan Plateau, suggesting that the Qiangtang block at longitude ~95° E accommodates east–west extensional crustal deformation by small-scale oblique normal faults, which may act as the boundary of micro-blocks. This may also mean that the normal faulting in the Qiangtang block is expanding outwards, and a new rifting system may be formed, which requires more geological evidence.

Keywords Normal faulting · 2016 Zaduo earthquake · Bayesian approach · Coulomb stress changes · Tibetan Plateau

1 Introduction

While the southern, northeastern, and eastern margins of the Tibetan Plateau are dominated by crustal shortening, tectonic activity in the interior of the plateau is characterized by roughly north–south crustal shortening and east–west crustal extension (Wang et al. 2001; Zhang et al. 2004; Meade 2007). These characteristics are evidenced by field investigations of active structures, satellite image analysis, geodetic observations, and fault plane solutions of earthquakes with normal and strike-slip faulting (Molnar and Lyoncaent 1989; Kapp et al. 2003; Deng et al. 2014). Recent Global Navigation Satellite System (GNSS) measurements show that the interior of the plateau is undergoing ESE–WNW extension at a rate of 22 ± 3 mm/year over ~ 2000 km (Zhang et al. 2004). The east–west extension of the Tibetan Plateau is manifested in a series of north–south and northeast–southwest trending grabens, especially in the central and southern Tibet (Armijo et al. 1986; Harrison et al. 1992). Meanwhile, the graben structure has been proved to play a significant control over the distribution of modern lakes and water systems in the plateau (Li et al. 2005). Analyses of earthquake focal mechanisms with dominant normal components indicate that earthquakes are almost entirely distributed at high elevations over 4000 m (Fig. 1a), suggesting that these features may be closely related to gravitational collapse of the Tibetan Plateau after achieving the maximum elevation (Molnar and Lyoncaent 1989; Harrison et al. 1992).

Elliott et al. (2010) used interferometric synthetic aperture radar (InSAR) and seismic waveform data to determine the faulting parameters for several normal faulting earthquakes that occurred in 2008 and found that all these events favored an angle dips over 40° rather than low-angle dips less than 30° and had a shallow focal depth of 10–15 km. The distribution of normal faulting earthquakes illustrates that there are a cluster of earthquakes ($4 < M_w < 6$) in the Qiangtang block between 92° E and 94° E (Fig. 1a), suggesting intense extensional deformation in this area. However, the eastward extent of normal faulting in the Qiangtang block is still uncertain. In this case, detailed investigations of coseismic slip models of a series of moderate-size normal fault earthquakes can complement our knowledge of crustal extension in the plateau. Additionally, the study of crustal deformation caused by earthquakes is important for a better understanding of seismic hazards and geological structure growth in tectonically active areas (Wu et al. 2018).

On 17 October 2016, an $M_s 6.2$ earthquake struck Zaduo county in southern Qinghai Province, China. The epicenter (32.81° N, 94.93° E) was at the western part of the intersection of the Zaduo-Shanglaxiu fault (F1) and Zaduo fault (F2), approximately 30 km from Zaduo county and 15 km from the nearest town Aduo (Fig. 1b). A field investigation conducted immediately after the shock indicated that no clear surface ruptures were found in the epicenter region. Since this event occurred in a relatively remote border region with sparse population, no casualties and major property losses were reported. Four $M > 4$ aftershocks (Fig. 1c) were recorded according to the United States Geological Survey (USGS: <https://earthquake.usgs.gov/earthquakes/search>), including the largest event ($M 4.7$) that occurred 20 min after the mainshock. At least 200 aftershocks were relocated within 40 days following the Zaduo mainshock (Jiang et al. 2018), and these aftershocks were distributed in the east–west direction along the Zaduo-Shanglaxiu fault (Fig. 1c). There were some differences between focal mechanism solutions determined by different organizations (Table S1). For instance, the result from the USGS indicated that it was a pure normal-faulting event, whereas the Global Centroid Moment Tensor (GCMT: <http://www.globalcmt.org>) and the Institute of Geophysics of China Earthquake Administration (IGPCEA: <http://news.ceic.ac.cn/>) showed that the earthquake was a predominantly normal slip accompanied by a minor strike-slip component. Moreover, the located focal depth differed between different agencies, varying from 9 to 35 km.

The exact mechanism of the Zaduo earthquake is not yet clear until now for its relatively small magnitude and the lack of available observation data. However, this event provides a rare opportunity to study the deformation of the Zaduo area, as it is the largest event recorded in the instrument catalog in the past 40 years. Previous studies (Qiu and Qiao 2017; Chen et al. 2018; Jiang et al. 2018) focused primarily on the coseismic slip model of the earthquake, but did not systematically examine its seismic mechanism or its implication for the crustal extension in the Tibetan Plateau. Different from Qiu et al. (2017) and Chen et al. (2018) employing the ascending InSAR measurements alone, we adopt both the ascending and descending InSAR observation data to determine the earthquake mechanism of the 2016 Zaduo event comprehensively. This event also provides a rare opportunity to gain insights into how stress

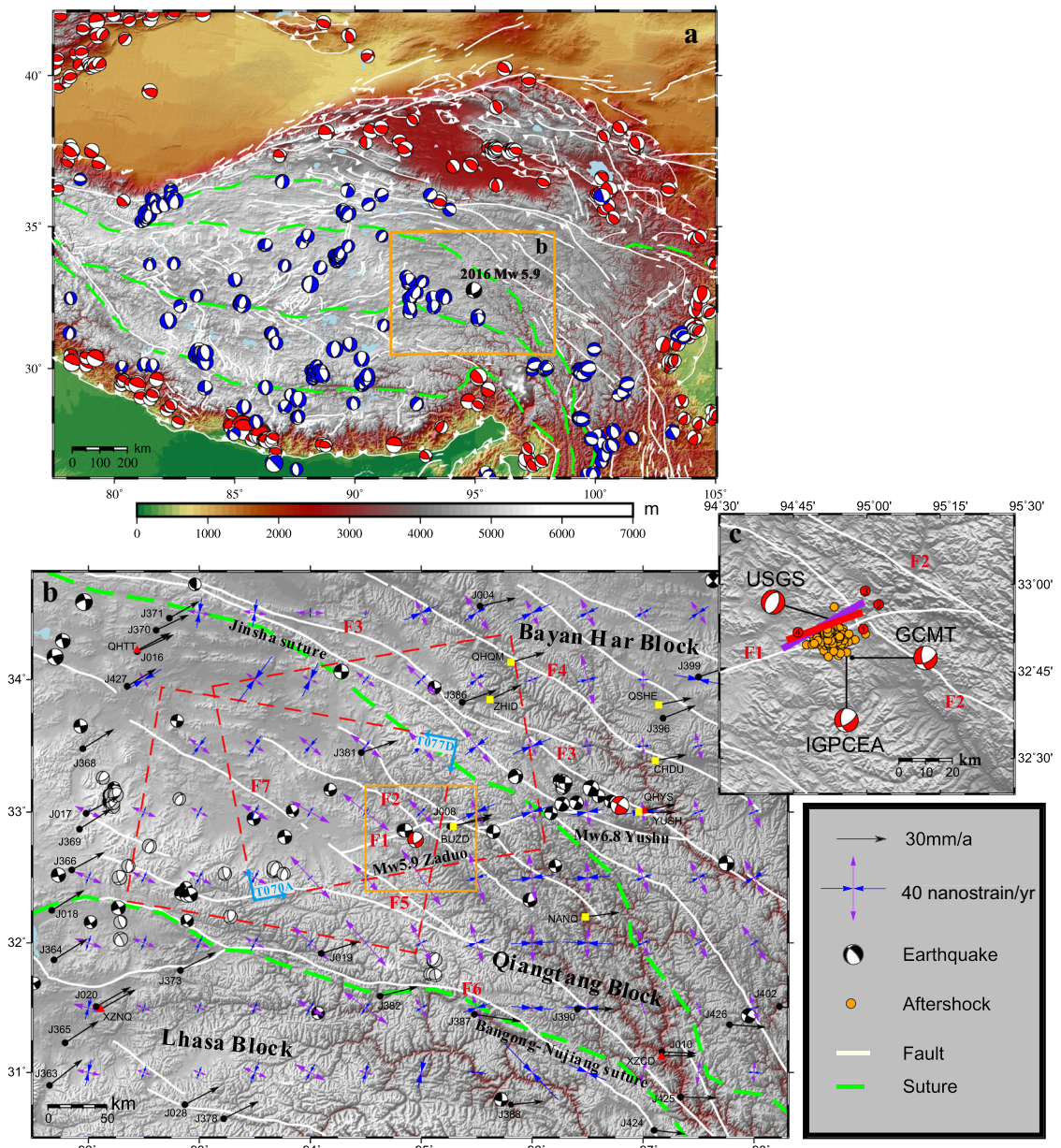


Fig. 1 Topographic and regional tectonic settings surrounding the 2016 Mw 5.9 Zaduo earthquake. **a** Normal faulting (blue beach ball) and reverse faulting (red beach ball) earthquakes located in the Tibetan Plateau from the GCMT catalog. **b** Two red beach balls denote GCMT focal mechanisms of the 2010 Mw 6.9 Yushu and 2016 Mw 5.9 Zaduo earthquake, respectively, whereas the black (strike-slip) and gray (normal) ones represent the focal mechanism of historical earthquakes in past 40 years taken from the GCMT catalog. Black vectors represent interseismic velocities relative to the Eurasian reference frame (Table S2). Purple and blue vectors indicate the extensional and compressional principal strain rates, respectively. Thick white lines delineate the main active faults. Red dashed rectangles outline the spatial coverage of the ascending and descending track of Sentinel-1A/B InSAR

data. Green thick dotted lines depict the Jinsha and Bangong-Nujiang sutures. The orange box indicates the central area of the Zaduo event and its adjacent tectonic belts (Fig. 1c). **c** Focal mechanism solutions are from the USGS, GCMT, and IGPCEA. The solid red line indicates the surface projection of the upper boundary of the preferred fault plane of this study, whereas the purple line represents the result of the modeled rupture fault from Jiang et al. (2018). The small orange circles denote aftershocks relocated within 40 days and the red dots indicate four aftershocks with magnitudes greater than 4 with numbers in the circle showing the order of the four aftershocks. F1, Zaduo-Shanglaxiu fault; F2, Zaduo fault; F3, Ganzi-Yushu fault; F4, Wudaoliang-Qumalai fault; F5, Niri Acuo Gai-Baqing fault; F6, Nujiang fault; and F7, Yanshiping fault

accumulates in the Qiangtang block as the Indian Plate collides with the Eurasian Plate. Interseismic velocities (Table S2) between 1998 and 2016 are re-calculated using the latest GNSS observations in this region ([Appendix](#)), which contains more newly built GNSS stations and has a longer observation time span compared with the existing results (Liang et al. 2013). The area's tectonic background is analyzed by using the interseismic observation data, which helps to determine the fault plane strike direction of the Zaduo earthquake. GNSS and InSAR data are used to obtain the interseismic crustal strain rate tensor and coseismic surface displacements associated with this earthquake, respectively. In addition, a Mw 6.9 earthquake occurred in the surrounding area in 2010, and it is worth discussing whether the Zaduo event is related to this historical earthquake. After the 2016 Zaduo mainshock, earthquakes with $M > 3$ occurred frequently in this area during 2017 to 2019, among which the latest one was the M 3.7 shock on September 9, 2019. Therefore, the detailed analysis of the seismogenic tectonic background of the 2016 Zaduo earthquake is helpful to understand the regional seismic risk.

In this paper, we first exploit the ascending and descending InSAR observations from Sentinel-1A/B satellites to depict the coseismic deformation fields of the Zaduo earthquake. Subsequently, we determine the optimal seismogenic fault geometry by a Bayesian approach, which is implemented using a Markov Chain Monte Carlo (MCMC) method, and aided by the principal axes of strain rate tensors, regional geological structure, and relocated aftershocks. The strain rate tensors are derived from the latest velocities between 1998 and 2016, including several our own stations ([Appendix](#), Table S2). Furthermore, we invert the optimal coseismic slip distribution of the Zaduo earthquake and calculate the coseismic and postseismic Coulomb stress disturbance caused by the 2010 Mw 6.9 Yushu earthquake. Finally, the tectonic implications in the interior of the Tibetan Plateau are discussed.

2 Datasets and processing

Geodetic data, e.g., GNSS and InSAR, have been widely used to investigate coseismic ground deformation caused by shallow crustal earthquakes and have a great advantage as they are more sensitive to fault geometry and slip distribution, especially in the case with shallow focal depths (Jónsson et al. 2002; Guo et al. 2019; Param et al. 2019). Although we have collected new GNSS measurement data in this area, it remains challenging to obtain detailed coseismic displacements directly even for moderate earthquakes, such as the Zaduo event. No substantial coseismic offsets were recorded from position time series by the two nearest GNSS stations calculated using the Bernese GNSS software version 5.2, which were the continuous station BUZD with station-epicenter distance of ~ 34 km, and the campaign-mode station J008 with ~ 30 km from the epicenter (Fig. 1b). Meanwhile, InSAR technology has been proven to be useful in acquiring continuous coseismic deformation, especially for moderate earthquakes in the Tibetan Plateau as a result of the severe environment for inconvenient access (Elliott et al. 2010; Sun et al. 2013; Bie et al. 2014). By combining satellite date acquired before and after an earthquake, InSAR provides spatially dense measurements of surface displacement, which play a crucial role in estimating and understanding crustal deformation and seismic hazard (Sudhaus and Sigurjón 2009; Amey et al. 2018).

2.1 InSAR observations

C-band (wavelength of ~ 5.6 cm) SAR images from the European Space Agency (ESA) Sentinel-1A/B satellites, which provide unprecedented revisit interval, were used to measure the coseismic deformation. Here, we first utilized the ascending and descending Sentinel-1A/B SAR interferograms (Table 1) of the 2016 Zaduo earthquake to image the surface displacements. We selected SAR acquisition pairs with the shortest spatial

Table 1 Sentinel-1A/B image data used in this study

Imaging model	Track	Master	Slave	Bperp (m)	ΔT (days)	Inc (°)	Azi (°)
IW	T070A	2016/09/29	2016/10/23	78	24	40.05	-10.16
IW	T077D	2016/09/17	2016/10/17	31	30	33.59	-169.24

A and *D* in the Track represent the ascending and descending orbits, respectively. *IW*, interferometric wide swath mode; *Bperp*, perpendicular baseline; ΔT , temporal baseline; *Inc*, incidence angle; *Azi*, azimuth angle

and temporal baselines to maximize the interferogram coherence. Short perpendicular baselines in the image pairs can reduce errors caused by the digital elevation model (DEM) and possible of spatial decorrelation (Simons et al. 2002). Additionally, image pairs with the shortest temporal baseline can decrease the postseismic deformation effects (Xu et al. 2015; Qiu et al. 2019).

We processed the InSAR data with GAMMA software (GAMMA Remote Sensing, Gümmligen, Switzerland) (Werner et al. 2002) to generate interferograms of the two image pairs for multi-looked by 10 looks in range and 2 looks in azimuth to improve the efficiency of calculation and reduce the noise of data points. A 3-arc-second (90 m) Shuttle Radar Topography Mission (SRTM) DEM (Farr et al. 2007) and precise orbital determination were utilized to flatten each interferogram to simulate and eliminate the topographic signals. Phase unwrapping was performed using the minimum cost flow algorithm (Chen and Zebker 2000) after reducing phase noise in flattened interferograms using a power spectrum filter (Werner et al. 2002). Finally, the interferograms were geocoded to a graphical coordinate system.

The interferometric fringes are basically continuous due to the short temporal interval and spatial baselines. The coseismic deformation pattern is similar for both ascending (T070A) and descending (T077D)

interferograms, indicating that the dominant coseismic displacement is subsidence in the vertical direction (Fig. 2), which is consistent with the focal mechanism dominated by normal slip. A maximum coseismic line-of-sight (LOS) displacement of ~4 cm was obtained from the approximate elliptical deformation area.

2.2 Estimation of InSAR data errors

InSAR images are usually contaminated by widespread atmospheric artifacts, which are spatially correlated (Parsons et al. 2006; Sudhaus and Sigurjón 2009; Amey et al. 2018). Therefore, InSAR data errors are particular for each InSAR image relating to the state of the atmosphere and ground surface at the time of the two radar acquisitions times. To construct the full covariance matrix of the noise, we selected a non-deforming area of the interferogram assuming that the error statistics are the same as those in the adjacent deforming areas, and then calculated the unbounded exponential 1-D semivariogram using a nugget model following the method of Bagnardi et al. (2018).

First, we removed a linear ramp from the original data to correct for possible long-wavelength atmospheric effects. Then the experimental semivariogram on the detrended datasets was estimated. Finally, the exponential function was fitted using a nugget model. We directly

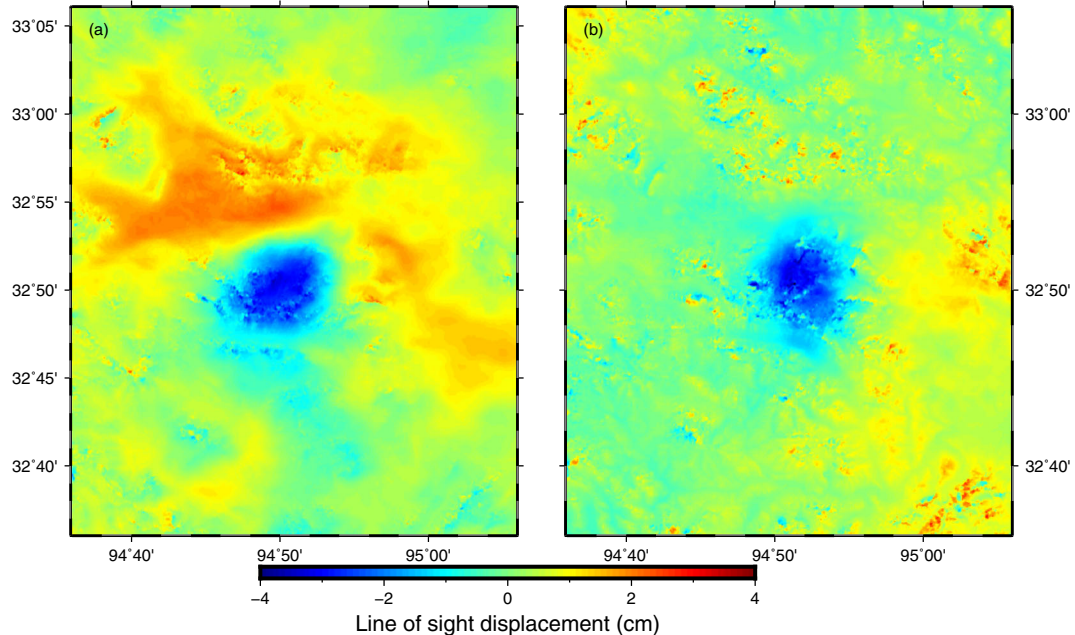


Fig. 2 The InSAR coseismic deformation fields from ascending (a) and descending (b) orbits used in this study. Negative values denote ground motion away from the satellite

characterized the errors in the InSAR datasets by experimentally estimating variance and covariance for each independent image, and the variance–covariance matrix using the exponential function is defined as:

$$C(h) \begin{cases} \text{sill} & h = 0 \\ \text{nugget} + (\text{sill} - \text{nugget}) \cdot e^{-\frac{|h|}{\text{range}}} & h > 0 \end{cases} \quad (1)$$

where $C(h)$ is the covariance at any given distance h between each InSAR dataset point; range is the distance over which data points are expected to be spatially correlated; nugget indicates the level of spatially independent noise, and sill is the maximum value of semivariance as the range tends toward infinity. A small range means that the covariance between data points will extend to a small distance. According to Eq. (1), the error characteristics of the ascending and descending InSAR data were calculated, respectively (Fig. 3). The results show that a higher auto-covariance value appears at distances of less than 2 km (Table 2).

3 Fault geometry and coseismic slip model

The ascending and descending unwrapped interferograms were subsampled using a quadtree decomposition algorithm (Jónsson et al. 2002), which is an irregular subsampling method that samples target region of an image more densely to capture the deformation signal details (Bagnardi and Hooper 2018). This method can subsample a reasonable number of data points and provide a good spatial representation of LOS displacements.

3.1 Optimal fault geometry parameters

Since no visible surface ruptures were found during the field investigation conducted after the Zaduo event, it is impossible to infer the location and strike of the rupture fault directly from geological investigations and InSAR images. The fault geometry, especially for a blind fault, is also difficult to be determined from the space geodetic data alone (Jiang et al. 2018; Xiong et al. 2018a). In such cases, relocated aftershocks sequences, geological structures, and other information are typically used to provide additional constraints on the fault geometry at depth. From Fig. 1c, the active tectonic map shows that the 2016 Zaduo earthquake occurred at the intersection of the NE trending Zaduo-Shanglaxiu (F1) fault and the NW oriented Zaduo fault (F2). According to the results

of three different focal mechanism solutions (Table S1), it is indicated that the Zaduo earthquake is characterized by a predominantly normal component, which is consistent with the results of InSAR deformation with a mainly subsidence in the center of the images. Geological research results show that the Zaduo fault is a sinistral transpressional slip zone with thrust components (Deng et al. 2014), so the earthquake is unlikely to occur on the F2 fault. Meanwhile, the latest GNSS strain rate tensor we calculated show that the epicentral area present a trend of NW–SE extension, which is consistent with the focal mechanism solutions. After the Zaduo mainshock, the track of four $M > 4$ aftershocks shows that the aftershocks first move to the east, then to the northeast, and finally to the west, basically along the strike of F1 fault. The aftershocks within 40 days after the Zaduo earthquake show that it is almost parallel to the distribution of F1 fault. In conclusion, it is considered that the most possible seismogenic fault of the Zaduo earthquake is related to the NE–SW trending F1 fault. Combined with the result of GCMT source mechanism solution (strike 63° , dip 59° , rake -33°), it is shown that the seismogenic fault is NE trending, which provide constraints for the subsequent estimation. Therefore, we consider that the most possible seismogenic fault is related to the southeast dipping F1 fault, aided by local geological structures, relocated distribution of aftershocks, focal mechanisms, and principal axes of strain rate tensors derived from our latest GNSS velocities.

To further determine the optimal fault parameters from the near-field InSAR data, we utilized a Bayesian approach to retrieve optimal source parameters and associated uncertainties of the Zaduo earthquake, which uses a posterior probability density function (PDF) to characterize the parameters of the source model (Sudhaus and Sigurjón 2009; Bagnardi and Hooper 2018; Amey et al. 2018). The Bayesian inversion algorithm efficiently samples posterior PDFs through a MCMC method (Mosegaard and Tarantola 1995) incorporating the Metropolis-Hastings algorithm (Hastings 1970). The inversion was carried out using a kinematic forward model for a rectangular dislocation source with nine parameters (Okada 1985). Prior fault geometry information was derived from previous studies (Table S1), and the source model parameters constraints are listed in Table 3. We discarded the first 50,000 samples as a burn-in period after $\sim 10^6$ iterations and regarded the subsequent samples drawn from the posterior PDF. The 2.5% and 97.5% confidence intervals of

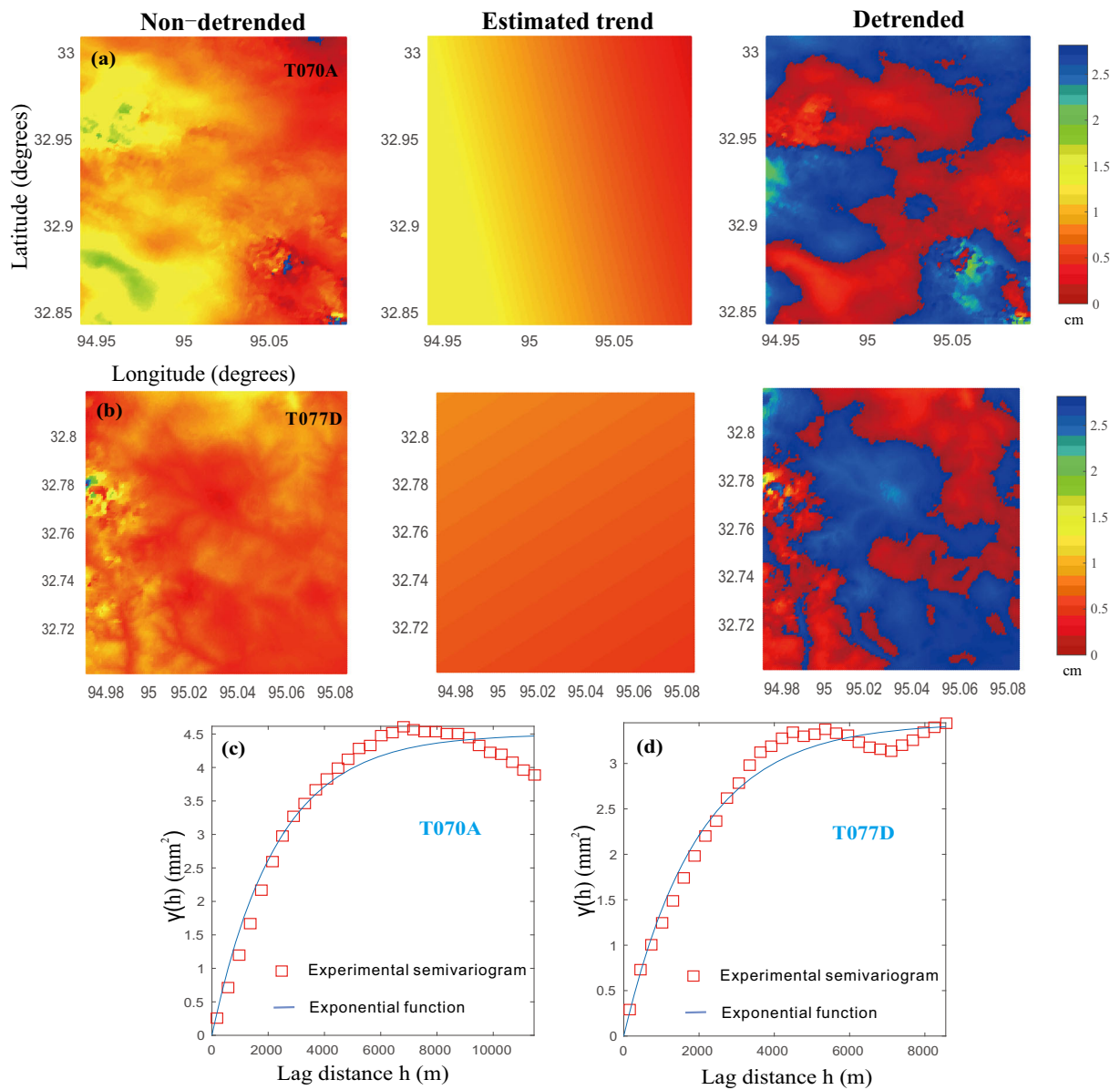


Fig. 3 Estimation of error characteristics in a non-deforming area from the ascending (a) and descending (b) InSAR data. Panels (c) and (d) show the experimental (red squares) and theoretical (blue line) semivariograms for the two Sentinel InSAR datasets, respectively

PDFs for all parameters are listed in Table 3. Figure 4 displays the marginal posterior distributions for estimated parameters, and the bottom panels show the

Table 2 Parameters of the theoretical exponential function

Track	Sill (m ²)	Nugget (m ²)	Range distance (m)
T070A	4.5×10^{-6}	4.6×10^{-18}	2291
T077D	3.4×10^{-6}	7.7×10^{-16}	1955

histograms of marginal distribution for each parameter as well as the optimal fault geometry determined by Jiang et al. (2018) for comparison. Some of the parameters have relatively broad marginal distribution peaks and some degree of asymmetry. The best-fitting fault plane has a southeast dip of $\sim 60^\circ$ and a northeast strike of $\sim 73^\circ$. This model favors dominant normal slip with a minor left-lateral strike-slip component. The predicted InSAR images from the maximum posterior probability solution show good agreement with the ascending and

Table 3 Prior information and inversion results of fault parameters for the 2016 Mw 5.9 Zaduo earthquake

	Length (km)	Width (km)	Depth (km)	Dip (°)	Strike (°)	X-center (km)	Y-center (km)	SS (m)	DS (m)
Lower	1	1	1	40	40	-5	-5	-0.5	-0.5
Upper	20	15	20	90	90	5	5	0	0
Start	5	5	10	65	65	0	0	-0.1	-0.1
Step	0.05	0.05	0.5	1	1	0.1	0.1	0.01	0.01
Optimal	7.47	5.82	11.24	60	73	1.35	-1.7	-0.13	-0.32
2.5%	5.25	3.13	9.72	55	69	0.79	-3.25	-0.19	-0.49
97.5%	8.63	8.99	12.83	65	76	1.77	-0.89	-0.03	-0.22

SS and DS represent strike-slip and dip-slip components, respectively. Note that the right-lateral SS is positive while left-lateral SS is negative. DS is positive for thrust faulting and negative for normal faulting. X and Y center means the coordinates of the midpoint of the lower edge related to the reference point (32.87° N, 94.87° E) in the local coordinates system

descending InSAR observations (Fig. S1). Most of the residuals in the earthquake rupture zone are small, and the mean residuals for the ascending and descending images are approximately 0.9 and 1.2 cm, respectively.

3.2 Finite fault slip model

To constrain the coseismic slip distribution, we first extended the optimal fault plane's length and width in

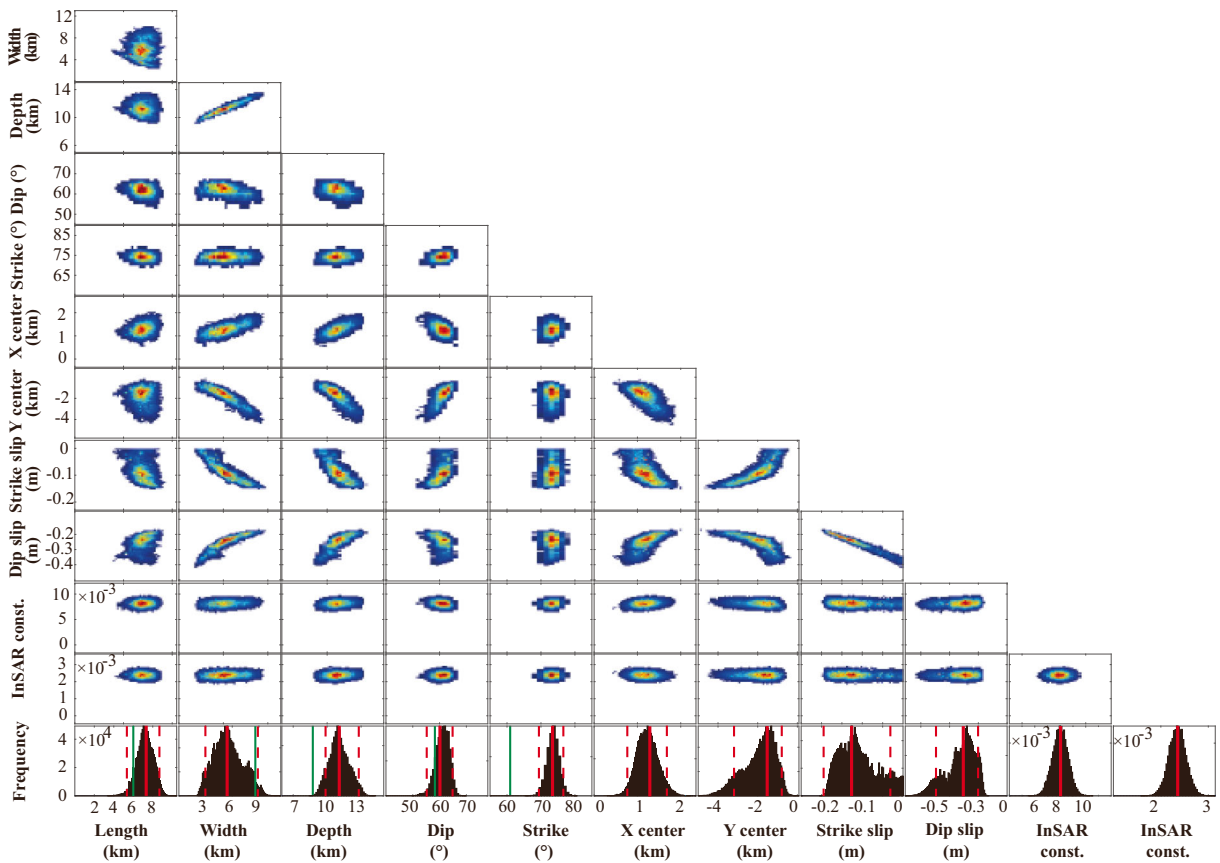


Fig. 4 Marginal posterior probability distributions of fault geometrical parameters for the 2016 Mw 5.9 Zaduo earthquake. The scatter plots indicate occurrence frequency, with warm colors denoting high frequency and cold colors denoting low frequency.

Bottom row: Histograms of model parameters; the best models are shown in thick red line with 95% confidence interval bounds in red dashed lines. The green lines show the source parameters obtained by Jiang et al. (2018)

the strike and dip directions to 30 km and 20 km, respectively. The strike and dip angles are fixed to the optimal fault geometry values (Table 3). The extended fault plane was discretized into 600 patches with a patch size of 1 km × 1 km. We linearly inverted for the slip distribution of the Zaduo earthquake using rectangular dislocation in an elastic half-space homogeneous dislocation model (Okada 1985) with a Poisson's ratio of 0.25. To obtain a physically realistic slip distribution, we employed Laplacian smoothing. We also used a smoothing factor empirically determined using an L-curve approach (Fig. S2). Considering 30 GPa for the shear modulus, we estimated a seismic moment of 7.45×10^{17} Nm. This corresponds to an event of Mw 5.92, which is in agreement with the previous solutions (Table S1). Figure 5 illustrates that the coseismic slip concentrates at a depth of 4–15 km, with a peak slip of ~24.7 cm. The resolved slip on the fault patches near the surface may indicate no ground ruptures, which was the situation observed by the geological field investigation (Jiang et al. 2018). Aftershocks are located in the periphery of the slip rupture (Fig. S3), and more than 90% are distributed at depths of 5–13 km, which is consistent with the mainshock rupture depth. InSAR downsampled observations are in good agreement with the simulated values, and the overall residuals are small (Fig. S4).

4 Discussion

4.1 The impact of the 2010 Mw 6.9 Yushu earthquake

Earthquake triggering by static and postseismic Coulomb stress changes has been testified and documented extensively around the world and is of great significance in the assessment of seismic hazard (Freed and Lin 2001; Pollitz and Sacks 2002; Durand et al. 2010).

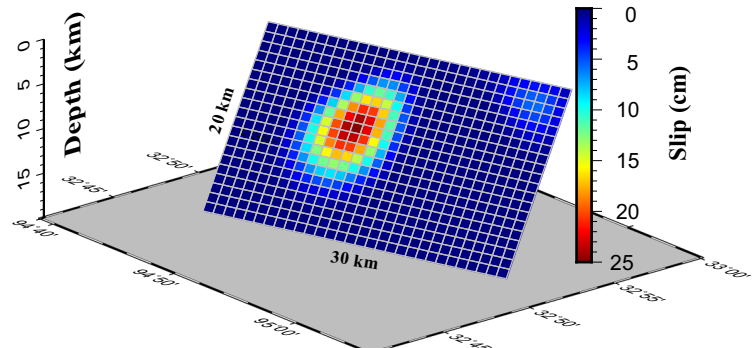
Fig. 5 Three-dimensional diagram of the coseismic slip distribution of the Zaduo earthquake derived from InSAR observations

Regions with stress increases of more than 0.1 bar (10 kPa) can be sufficient to trigger seismic activities and sometimes induce aseismic slow slip remotely, which may increase the seismic risks in the surrounding area (Stein 1999; Zhao et al. 2018). Here, we investigate whether the occurrence of the 2016 Zaduo earthquake could be delayed triggering by the 2010 Mw 6.9 Yushu earthquake, which ruptured on the northwestern segment of the sinistral strike-slip Ganzi-Yushu fault (Shan et al. 2011; Sun et al. 2013; Wang et al. 2013; Xiong et al. 2018a). The horizontal distance between these two events is approximately 160 km. Based on the Coulomb failure criterion, the Coulomb Failure Stress change (ΔCFS) is defined as (Scholz 1990):

$$\Delta\text{CFS} = \Delta\tau - \mu\Delta\sigma_n \quad (2)$$

where ΔCFS is the Coulomb failure stress change calculated on a specific receiver fault; $\Delta\tau$ and $\Delta\sigma_n$ are the changes in shear and effective normal stress acting on the receiver fault, respectively; and μ represents for the effective friction coefficient.

To evaluate the time-dependent Coulomb stress changes due to the 2010 Yushu earthquake, we assumed a laterally homogeneous viscoelastic stratification consisting of an elastic upper crust underlain by ductile lower crust and upper mantle. Considering the viscosity of the lower crust and upper mantle in this region is poorly constrained, we adopted a linear Maxwell rheology and investigated several representative viscosity values (Table S3). The receiver fault is assumed to have a strike of 73°, a dip of 60°, and a rake of –65° according to the fault geometry values obtained in this study. We used the PSGRN/PSCMP software package (Wang et al. 2006) to calculate the coseismic and postseismic Coulomb stress changes at the epicenter of 2016 Zaduo earthquake using the InSAR-derived coseismic slip model of the 2010 Yushu earthquake (Sun et al. 2013). Figure 6 illustrates



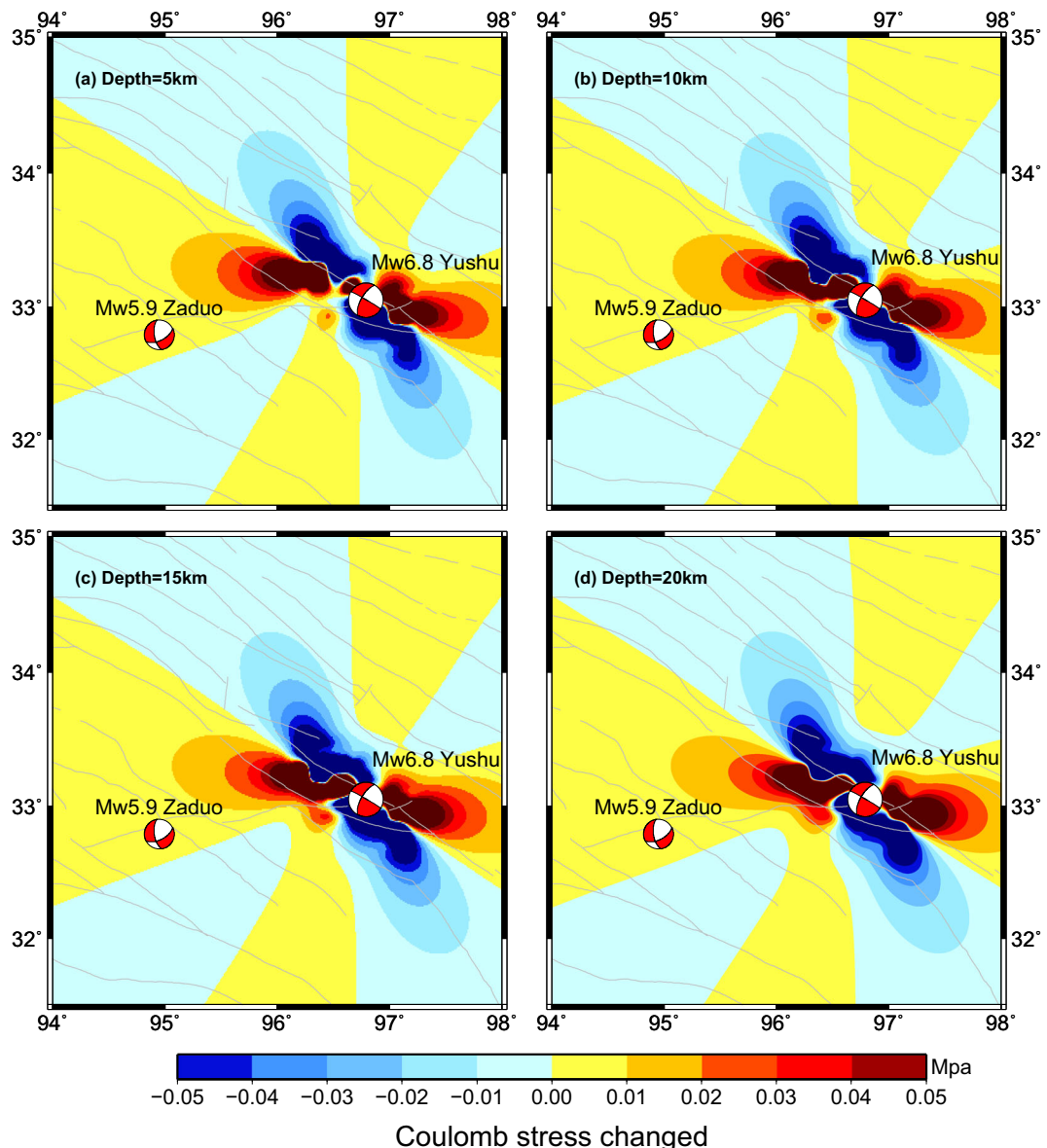


Fig. 6 Coseismic and postseismic Coulomb stress changes for a receiver fault aligned with the 2016 Zaduo earthquake rupture surface caused by the 2010 Mw 6.9 Yushu earthquake at different

depths of 5 km (a), 10 km (b), 15 km (c), and 20 km (d). Warm and cool colors represent increased and decreased ΔCFS values, respectively

the cumulative Coulomb stress changes including the static and time-dependent ΔCFS at different depths of 5 km, 10 km, 15 km, and 20 km, calculated with a steady-state viscosity of 5×10^{17} Pas. The calculation of Coulomb stress indicates that the rupture of the 2010 Yushu event imposed Coulomb stress increases at different depths in the Zaduo area. The coseismic rupture of the Yushu earthquake resulted in a static Coulomb stress increase of 1.31 kPa at the epicenter of the 2016 Zaduo

earthquake (10 km). Up to the occurrence time of the Zaduo earthquake, the cumulative Coulomb stress increased by 3.10 kPa (Fig. 6b). The Coulomb stress changes caused by postseismic relaxation are comparable to those caused by the coseismic rupture, indicating that the postseismic relaxation cannot be neglected in delayed stress triggering.

Equation (2) shows that the value of the effective friction coefficient does not change ΔCFS trend for a

given receiving fault, but rather only affects the weight of normal stress (Shan et al. 2011; Xiong et al. 2018b). While the viscosity of lower crust and upper mantle affects the relaxation time and Coulomb stress calculation, the cumulative Coulomb stress increase varies from 2.7 to 3.4 kPa with viscosity values of 1×10^{18} Pas and 1×10^{17} Pas, respectively (Fig. 7). A lower viscosity yields a larger postseismic Coulomb stress changes (and vice versa). The steady-state viscosity of the lower crust beneath the Tibetan Plateau probed by investigating postseismic displacements is usually larger than 1×10^{17} Pas (Huang et al. 2014; Zhao et al. 2017). This means that the calculated ACFS of 3.4 kPa gives an upper bound value for the delayed stress triggering. The cumulative Coulomb stress changes loaded by the coseismic and postseismic deformation caused by the Yushu earthquake are only up to 34% of the widely accepted thressed value of 0.1 bar (10 kPa), which probably indicates that the Zaduo earthquake was not triggered by the Yushu event. Of course, we cannot rule out that the occurrence time of the 2016 Zaduo earthquake could have been advanced by the 2010 Yushu earthquake.

4.2 Comparison to previous results

The earthquake mechanism of the 2016 Zaduo event affects the subsequent understanding of tectonic activity of the eastern Qiangtang block. Based on the regional tectonic background, the strain rate tensor we derived and

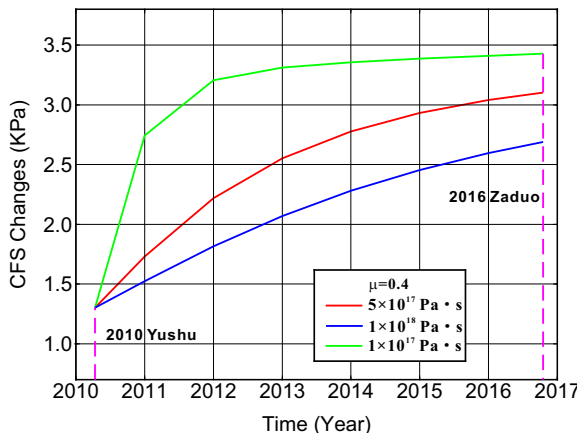


Fig. 7 Evolution of Coulomb stress changes at the hypocenter of the 2016 Zaduo earthquake caused by the 2010 Yushu earthquake. Dotted pink lines indicate the occurrence times of the 2010 Yushu and 2016 Zaduo earthquakes, respectively. Color-coded curves represent the time-dependent CFS due to postseismic relaxation using different viscosities

the relocated aftershocks, we consider that the seismogenic fault of the Zaduo earthquake is probably related to the NE-trending F1 fault (Fig. 1c). This conclusion is basically consistent with the results from Jiang et al. (2018) and other studies (Qiu and Qiao 2017; Chen et al. 2018). However, there are some fault geometry discrepancies between the different coseismic slip models inferred from InSAR data and between focal mechanisms (Table S1). The strike directions obtained from different solutions vary from 58 to 73°. We favor the strike direction of 73°, which is derived from a large number of iterations using MCMC sampling rather than a small number of tests. Here, the fault geometrical parameters and their associated uncertainties were given through a Bayesian approach in this study (Table 3). The maximum coseismic slip of our model is smaller than that of Jiang et al. (2018) and larger than that of other models (Qiu and Qiao 2017; Chen et al. 2018), reflecting the different smoothing factors used in slip inversions.

In addition, the preferred fault plane we derived is nearly parallel to the F1 fault. The azimuth of the minimum principal axes of strain rate tensors at the epicenter is ~45°, which is smaller than the strike of the seismogenic fault. This difference maybe explain the relatively sinistral strike-slip component on the fault plane. All solutions favor high-angle dips rather than a low value, which is consistent with the analysis of Elliott et al. (2010). Our results denote that the 2016 Mw 5.9 Zaduo earthquake was an oblique normal event in the Tibetan Plateau. The normal fault characteristics of the Zaduo event indicate that the Qiangtang block may be composed of several sub-blocks with different eastward velocities.

4.3 Tectonic implications

The boundary of the Tibetan Plateau is dominated by crustal shortening along its southern and eastern edges and by strike-slip motion along its northern and south-eastern margins. Additionally, there are many well-developed normal faults in the interior plateau, especially in southern Tibet, as exemplified by moderate normal faulting earthquakes (Armijo et al. 1986; England and Houseman 1989; Ratschbacher et al. 1994; Yin et al. 1999; Elliott et al. 2010). The Qiangtang block is sandwiched between the Jinsha suture zone in the northern Tibetan Plateau and the Bangong-Nujiang suture zone in the southern Tibetan Plateau, narrowing gradually from west to east (Fig. 1b). The Bangong-Nujiang

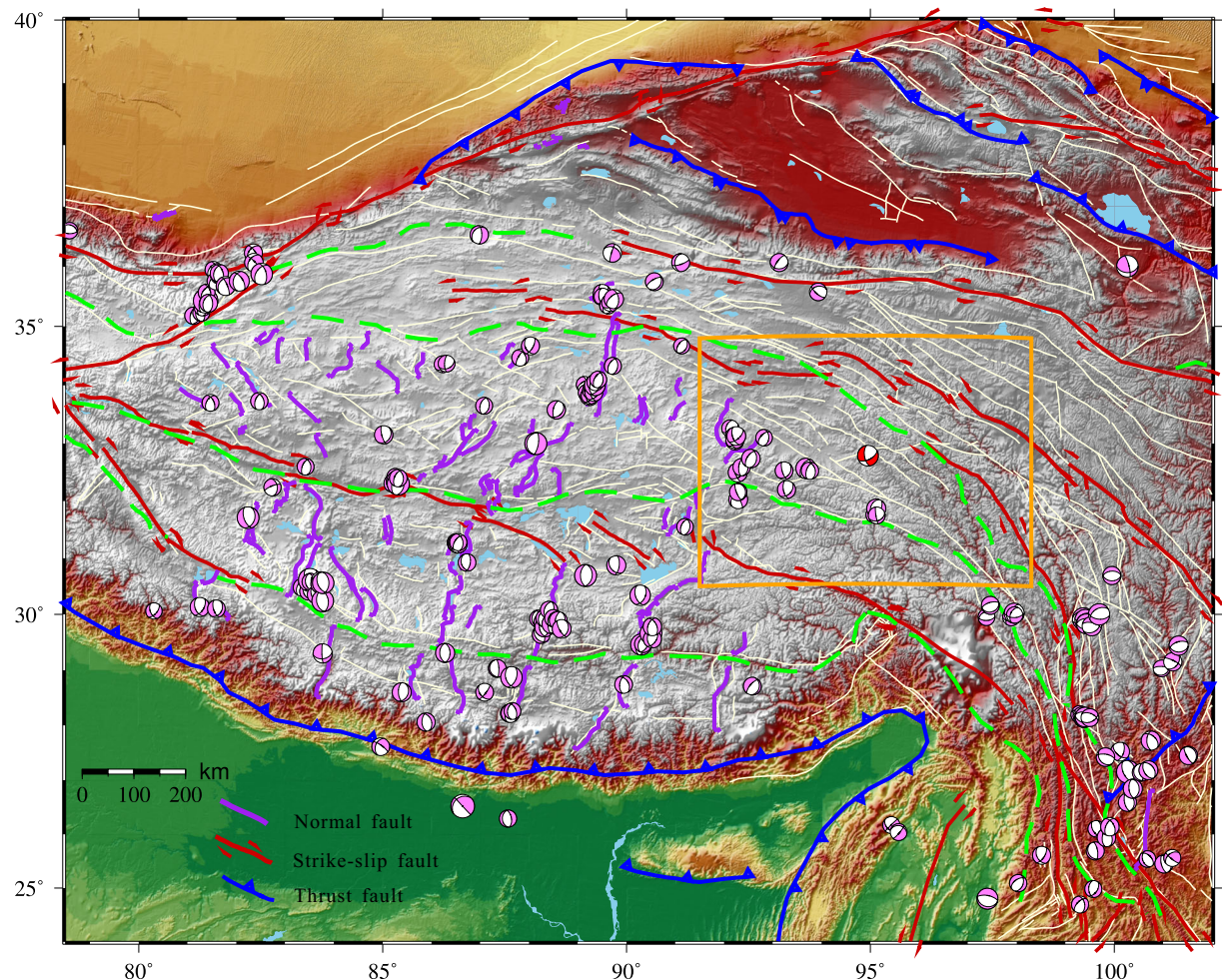


Fig. 8 Distribution of main active faults in the Tibetan Plateau. Beach balls reflect the normal faulting earthquake, as shown in Fig. 1

suture zone is a Mesozoic tectonic boundary in the central Tibetan Plateau that separates the Lhasa terrane to the south from the Qiangtang terrane to the north (Kapp et al. 2003; Sun et al. 2019). The Jinsha suture is part of the boundary fault zone between the Bayan Har block and the Qiangtang block, which plays an important role in regulating the eastward extrusion of the Tibetan Plateau. Understanding the formation of these normal fault earthquakes is of great significance for understanding the deformation model and dynamic processes of the Tibetan Plateau.

Widely distributed normal faulting earthquakes in the Tibetan Plateau have two features, high dip angles and shallow focal depths of 9–15 km, indicating that the brittle upper crust is thin in most of the seismogenic region of the plateau. The 2016 Zaduo earthquake occurred in the eastern part of the Qiangtang block at an

altitude greater than 4700 m, which belongs to the extensional tectonic region (Fig. 1a, b). Also, the normal faulting on the plateau maybe the result of variations in the gravitational potential energy of the lithosphere, which has been suggested by other researchers (Molnar et al. 1993; Elliott et al. 2010). Therefore, the extension of the interior plateau is clearly associated with topographic features and is driven primarily by gravitational forces. The latest GNSS results show that the proposed strain rate of the Qiangtang block increases significantly, which is consistent with the geological background of normal fault activity in the region. Current GNSS data do not allow us to explore the detailed strain partitioning within the Qiangtang block. However, previous block modeling ignoring the boundary at ~ 95° indeed left relatively large and systemically oriented residuals (Loveless and Meade 2011; Wang et al. 2017).

The rifting system in the Qiangtang block is not well developed compared with that in southern Tibet (Armijo et al. 1986; Blisniuk et al. 2001; Styron et al. 2015), implying that the rifting could be closely related to the progressive underthrusting of the Indian Plate beneath the Tibetan Plateau (Copley et al. 2011; Decelles et al. 2002). Previous active fault mapping in the central Tibetan Plateau has found no large-scale normal faults east of longitude $\sim 93^\circ$ E (Taylor and Yin 2009). However, there has been a cluster of normal faulting earthquakes in the eastern Qiangtang block east of longitude $\sim 93^\circ$ E, which suggests that either rifting systems are developing in this region or they were developed but not mapped previously (Fig. 8). The 2016 Mw 5.9 Zaduo earthquake is the largest instrument recorded normal faulting earthquake in the easternmost region of the Qiangtang block in past 40 years, indicating that the east–west extension of the Qiangtang block could extend to longitude $\sim 95^\circ$ E. The NE trending Zaduo-Shanglaxiu fault has been active in Quaternary but has not been active since late Pleistocene. The occurrence of the 2016 Zaduo earthquake may show that the fault recently has started to active. It also implies that the normal faulting in the interior Qiangtang block is expanding outwards and may form a new rift, which needs more evidence from geological research.

5 Conclusions

The 2016 Mw 5.9 Zaduo event provides an opportunity to probe the activity and tectonic context of the eastern Qiangtang block in the Tibetan Plateau. Here, we first analyze coseismic deformation associated with the Zaduo earthquake using ascending and descending Sentinel-1A/B radar images. We used a Bayesian estimation method to determine the posterior probability distribution of the model parameters and quantify its uncertainties. The obtained optimal seismogenic fault is probably the NE trending Zaduo-Shanglaxiu fault, which has a strike direction of $\sim 73^\circ$ and a dip angle of $\sim 60^\circ$. The observed elliptical subsidence with ~ 4 cm LOS displacement was caused by a peak slip of ~ 24.7 cm, consisting mostly of normal component and minor sinistral strike-slip motion. The cumulative Coulomb stress changes due to the coseismic and postseismic deformation of the nearby 2010 Mw 6.9 Yushu earthquake are far smaller than the typically accepted triggering threshold of 10 kPa. Therefore, the occurrence of

the Zaduo earthquake is probably a spontaneous event related to the dominant extensional strain accumulation rather than a delayed triggering event caused by the 2010 Mw 6.9 Yushu earthquake. Normal faulting and corresponding rifting system in the Qiangtang block maybe extending eastward, and probably even expand to longitude $\sim 95^\circ$ E.

Acknowledgments We are particularly indebted to the associate editor and two anonymous reviewers for their constructive comments, which have greatly improved the manuscript. The Sentinel-1A/B InSAR images used in this study were freely available and provided by Sentinels Scientific data Hub of Copernicus and European Space Agency. GNSS raw data were provided by the CMONOC Project (<ftp://cgsps.ac.cn>) and First institute of Surveying and Mapping of Qinghai Province, which were processed using Bernese GNSS software. The open-source Geodetic Bayesian Inversion Software were used to apply non-linear inversion for the fault geometry. The PSGRN/PSCMP packages were provided by Prof. Wang Rongjiang at GeoForschungsZentrum Potsdam(GFZ). The figures are partly generated by the Generic Mapping Tools (GMT) software package (Wessel et al. 2013).

Availability of data and materials The datasets used during the current study are available from the corresponding author on a reasonable request.

Authors' contributions JY and BZ conceived and designed the experiments. JY drafted the original manuscript. BZ led the research work, proposed the crucial suggestions of this manuscript. WX processed the InSAR data and commented on the manuscript. DW and KT contributed to funding acquisition. All authors read and approved the final manuscript.

Funding information This research was supported by the National Key Research and Development Program of China (grant number 2018YFC1503605); the Natural Science Foundation of Hubei Province (grant number 2019CFB794); and the Scientific Research Fund of Institute of Seismology and Institute of Crustal Dynamics, China Earthquake Administration (grant numbers IS201726172).

Compliance with ethical standards

Competing interests The authors declare that they have no competing interests.

Ethics approval and consent to participate Not applicable.

Abbreviations USGS, United States Geological Survey; GCMT, Global centroid moment tensor; IPGCEA, Institute of Geophysics of China Earthquake Administration; GNSS, Global navigation satellite system; InSAR, Interferometric synthetic aperture radar; CMONOC, Crustal Movement

Observation Network of China; *QHCORS*, Qinghai Continuously Operating Reference System; *MCMC*, Markov Chain Monte Carlo; *ESA*, European Space Agency; *DEM*, Digital elevation model; *SRTM*, Shuttle Radar Topography Mission; *LOS*, Line-of-sight; *PDF*, Posterior probability density function; *CFS*, Coulomb failure stress change

Appendix. GNSS data processing

To obtain the interseismic crustal movement in the region of the Zaduo earthquake, we collected observation data from 31 campaign GNSS stations of the Crustal Movement Observation Network of China (CMONOC) dotted by black solid balls which were surveyed between 1999 and 2016, 16 continuous GNSS stations from the CMONOC and Qinghai Continuously Operating Reference System (QHCORS) described with red triangles and yellow squares, respectively (Fig. 1b). Continuous stations from the CMONOC and the QHCORS began operating in 2010 and 2013, respectively. The survey-model campaign stations started operations in 1998, with an occupation of at least four consecutive days in each survey. Meanwhile, the nationwide campaign GNSS stations were observed regularly in 2009, 2011, 2013, and 2015 before the 2016 Zaduo earthquake.

All the GNSS data were processed using the latest Bernese GNSS software (version 5.2) developed at the Astronomical Institute of the University of Bern. It is a scientific, high-precision, multi-GNSS data-processing software package that can simultaneously process GPS and GLONASS observation data and supports Galileo satellite navigation system data processing in its latest update version (Yu et al. 2019). Firstly, we processed the observation data along with more than 30 IGS stations in and around the Chinese mainland using a double-difference approach to generate daily solutions. Then, the daily loosely constrained station coordinates were transformed to the ITRF2014 framework (Altamimi et al. 2016) using IGS core reference stations to define the seven-parameter Helmert transformations. Finally, station coordinates and velocities were estimated from position time series. To clearly show interior deformation within the Qiangtang block, interseismic velocities were presented in Table S2, which has transformed into the stable Eurasian reference frame, and the strain field (Fig. 1b) was calculated using a modified least-squares method iterated over a 2D space with

arbitrarily small increments to warrant solution continuity (Shen et al. 2015). The crustal strain field can better reflect the internal mechanism's response to crustal deformation and reveal its possible correlations with seismic activity (Qu et al. 2018).

References

- Altamimi Z, Rebischung P, Métivier L, Collilieux X (2016) ITRF2014: a new release of the international terrestrial reference frame modeling nonlinear station motions. *J Geophys Res Solid Earth* 121:6109–6131. <https://doi.org/10.1002/2016JB013098>
- Amey R, Hooper A, Walters R (2018) A Bayesian method for incorporating self-similarity into earthquake slip inversions. *J Geophys Res Solid Earth* 123:6052–6071. <https://doi.org/10.1029/2017JB015316>
- Armijo R, Tapponnier P, Mercier J, Han T (1986) Quaternary extension in southern Tibet: field observations and tectonic implications. *J Geophys Res Solid Earth* 91:13803–13872. <https://doi.org/10.1029/JB091iB14p13803>
- Bagnardi M, Hooper A (2018) Inversion of surface deformation data for rapid estimates of source parameters and uncertainties: a Bayesian approach. *Geochim Geophys Geosyst* 19:2194–2211. <https://doi.org/10.1029/2018GC007585>
- Bie L, Ryder I, Nippes S, Bürgmann R (2014) Coseismic and post-seismic activity associated with the 2008 Mw6.3 Damxung earthquake, Tibet, constrained by InSAR. *Geophys J Int* 196:788–803. <https://doi.org/10.1093/gji/ggt444>
- Blisniuk P, Hacker B, Glodny J, Ratschbacher L, Bi S, Wu Z, Calvert A (2001) Normal faulting in Central Tibet since at least 13.5 Myr ago. *Nature* 412:628–632
- Chen C, Zebker H (2000) Network approaches to two-dimensional phase unwrapping: intractability and two new algorithms. *J Opt Soc Am A* 17:401–414. <https://doi.org/10.1364/JOSAA.17.000401>
- Chen W, Yu P, Xiong W, Lin M (2018) The fault slip distribution of Zaduo Ms 6.2 earthquake as revealed by Sentinel-1 InSAR data. *J Geod Geodyn* 38:7380–7742. (In Chinese with English abstract). <https://doi.org/10.14075/j.jgg.2018.07.016>
- Copley A, Avouac J, Wernicke B (2011) Evidence for mechanical coupling and strong Indian lower crust beneath southern Tibet. *Nature* 472(79):79–81. <https://doi.org/10.1038/nature09926>
- DeCelles P, Robinson D, Zandt G (2002) Implications of shortening in the Himalayan fold-thrust belt for uplift of the Tibetan plateau. *Tectonics* 21:12–11. <https://doi.org/10.1029/2001TC001322>
- Deng Q, Chen S, Ma J, Du P (2014) Seismic activities and earthquake potential in the Tibetan plateau. *Chin J Geophys* 57(7):2025–2042. <https://doi.org/10.1002/cjg2.20133>
- Durand V, Bouchon M, Karabulut H, Marsan D, Schmittbuhl J, Bouin MP, Daniel G (2010) Seismic interaction and delayed

- triggering along the North Anatolian Fault. *Geophys Res Lett* 37(18). <https://doi.org/10.1029/2010GL044688>
- Elliott J, Walters R, England P, Jackson J, Li Z, Parsons B (2010) Extension on the Tibetan plateau: recent normal faulting measured by InSAR and body wave seismology. *Geophys J Int* 183:503–535
- England P, Houseman G (1989) Extension during continental convergence, with application to the Tibetan plateau. *J Geophys Res Solid Earth* 94:17561–17579. <https://doi.org/10.1029/JB094iB12p17561>
- Farr T, Rosen P, Caro E, Crippen R, Duren R, Hensley S, Kobrick M, Paller M, Rodriguez E, Roth L (2007) The shuttle radar topography mission. *Rev Geophys* 45(2). <https://doi.org/10.1029/2005RG000183>
- Freed A, Lin J (2001) Delayed triggering of the 1999 Hector mine earthquake by viscoelastic stress transfer. *Nature* 411:180–183. <https://doi.org/10.1038/35075548>
- Guo S, Zhang G, Zhu Y (2019) Gravity changes and crustal deformations before the Menyuan, Qinghai Ms6.4 earthquake of 2016. *Geodesy Geodyn* 10(4):315–320. <https://doi.org/10.1016/j.geog.2019.03.007>
- Harrison T, Copeland P, Kidd W, Yin A (1992) Raising Tibet. *Science* 255:1663–1670. <https://doi.org/10.1126/science.255.5052.1663>
- Hastings WK (1970) Monte Carlo sampling methods using Markov chains and their applications. *Biometrika* 57:97–109. <https://doi.org/10.1093/biomet/57.1.97>
- Huang M, Bürgmann R, Freed A (2014) Probing the lithospheric rheology across the eastern margin of the Tibetan plateau. *Eur Planet Sci Lett* 396:88–96
- Jiang G, Wen Y, Li K, Fang L, Xu C, Zhang Y, Xu X (2018) A NE-trending oblique-slip fault responsible for the 2016 Zaduo earthquake (Qinghai, China) revealed by InSAR data. *P Appl Geophys* 175:4275–4288
- Jónsson S, Zebker H, Segall P, Amelung F (2002) Fault slip distribution of the 1999 M w 7.1 Hector mine, California, earthquake, estimated from satellite radar and GPS measurements. *Bull Seismol Soc Am* 92(4):1377–1389
- Kapp P, Murphy M, Yin A, Harrison TM, Ding L, Guo J (2003) Mesozoic and Cenozoic tectonic evolution of the Shiquanhe area of western Tibet. *Tectonics* 22(4). <https://doi.org/10.1029/2001TC001332>
- Li Y, Wang C, Yi H, Li Y, Wang M (2005) A discussion on several problems regarding to the Cenozoic grabens in the Qinghai-Tibet plateau. *Geological Review* 52(5):493–501 (In Chinese with English abstract)
- Liang S, Gan W, Shen C, Xiao G, Liu J, Chen W, Ding X, Zhou D (2013) Three-dimensional velocity field of present-day crustal motion of the Tibetan plateau derived from GPS measurements. *J Geophys Res Solid Earth* 118:5722–5732. <https://doi.org/10.1002/2013JB010503>
- Loveless J, Meade B (2011) Spatial correlation of interseismic coupling and coseismic rupture extent of the 2011 Mw= 9.0 Tohoku-oki earthquake. *Geophys Res Lett* 38(17). <https://doi.org/10.1029/2011GL048561>
- Meade BJ (2007) Present-day kinematics at the India-Asia collision zone. *Geology* 35:81–84. <https://doi.org/10.1130/G22924A.1>
- Molnar P, Lyoncaent H (1989) Fault plane solutions of earthquakes and active tectonics of the Tibetan plateau and its margins. *Geophys J Int* 99:123–153
- Molnar P, England P, Martinod J (1993) Mantle dynamics, uplift of the Tibetan plateau, and the Indian monsoon. *Rev Geophys* 31:357–396
- Mosegaard K, Tarantola A (1995) Monte Carlo sampling of solutions to inverse problems. *J Geophys Res Solid Earth* 100:12431–12447
- Okada Y (1985) Surface deformation due to shear and tensile faults in a half-space. *Bull Seismol Soc Am* 75(4):1135–1154
- Param K, Rajesh S, John P, Naresh K, Arkoprovo B, George P, Chandra P (2019) GPS measured static and kinematic offsets at near and far field of the 2011 mw 9.0 Tohoku-Oki earthquake. *Geodesy Geodyn* 10(3):213–227. <https://doi.org/10.1016/j.geog.2019.03.003>
- Parsons B, Wright T, Rowe P, Andrews J, Jackson J, Walker R, Khatib M, Talebian M, Bergman E, Engdahl E (2006) The 1994 Sefidabeh (eastern Iran) earthquakes revisited: new evidence from satellite radar interferometry and carbonate dating about the growth of an active fold above a blind thrust fault. *Geophys J Int* 164:202–217. <https://doi.org/10.1111/j.1365-246X.2005.02655.x>
- Pollitz F, Sacks I (2002) Stress triggering of the 1999 Hector mine earthquake by transient deformation following the 1992 Landers earthquake. *Bull Seismol Soc Am* 92:1487–1496. <https://doi.org/10.1785/0120000918>
- Qiu J, Qiao X (2017) A study on the seismogenic structure of the 2016 Zaduo, Qinghai Ms6.2 earthquake using InSAR technology. *Geodesy Geodyn* 8(5):342–346. <https://doi.org/10.1016/j.geog.2017.04.008>
- Qiu J, Liu L, Wang C, Wang Y (2019) Present-day tectonic activity along the central section of the Altyn Tagh fault derived from time series InSAR. *Geodesy Geodyn* 10(4):307–314. <https://doi.org/10.1016/j.geog.2019.03.008>
- Qu W, Lu Z, Zhang Q, Hao M, Wang Q, Qu F, Zhu W (2018) Present-day crustal deformation characteristics of the southeastern Tibetan plateau and surrounding areas by using GPS analysis. *J Asian Earth Sci* 163:22–31. <https://doi.org/10.1016/j.jseas.2018.05.021>
- Ratschbacher L, Frisch W, Liu G, Chen C (1994) Distributed deformation in southern and western Tibet during and after the India-Asia collision. *J Geophys Res Solid Earth* 99:19917–19945. <https://doi.org/10.1029/94JB00932>
- Scholz C (1990) The mechanics of earthquakes and faulting. Cambridge University Press, New York, p 439
- Shan B, Xiong X, Zheng Y, Wei S, Wen Y, Jin B, Ge C (2011) The co-seismic Coulomb stress change and expected seismicity rate caused by 14 April 2010 Ms=7.1 Yushu, China, earthquake. *Tectonophysics* 510:345–353
- Shen ZK, Wang M, Zeng Y, Wang F (2015) Optimal interpolation of spatially discretized geodetic data. *Bull Seismol Soc Am* 105(4):2117–2127
- Simons M, Fialko Y, Rivera L (2002) Coseismic deformation from the 1999 M w 7.1 Hector mine, California, earthquake as inferred from InSAR and GPS observations. *Bull Seismol Soc Am* 92:1390–1402
- Stein R (1999) The role of stress transfer in earthquake occurrence. *Nature* 402:605–609. <https://doi.org/10.1038/45144>
- Styron R, Taylor M, Sundell K (2015) Accelerated extension of Tibet linked to the northward underthrusting of Indian crust. *Nat Geosci* 8(2):131–134
- Sudhaus H, Sigurjón J (2009) Improved source modelling through combined use of InSAR and GPS under consideration of

- correlated data errors: application to the June 2000 Kleifarvatn earthquake, Iceland. *Geophys J Int* 176:389–404
- Sun J, Shen Z, Bürgmann R, Wang M, Chen L, Xu X (2013) A three-step maximum a posteriori probability method for InSAR data inversion of coseismic rupture with application to the 14 April 2010 mw 6.9 Yushu, China, earthquake. *J Geophys Res Solid Earth* 118(8):4599–4627. <https://doi.org/10.1002/jgrb.50244>
- Sun G, Hu X, Xu Y, Bou M (2019) Discovery of middle Jurassic trench deposits in the Bangong-Nujiang suture zone: implications for the timing of Lhasa-Qiangtang initial collision. *Tectonophysics* 750:344–358
- Taylor M, Yin A (2009) Active structures of the Himalayan-Tibetan orogen and their relationships to earthquake distribution, contemporary strain field, and Cenozoic volcanism. *Geosphere* 5:199–214
- Wang Q, Zhang P, Freymueller J, Bilham R, Larson K, Lai X, You X, Niu Z, Wu J, Li Y, Liu J, Yang Z, Chen Q (2001) Present-day crustal deformation in China constrained by global positioning system measurements. *Science* 294:574–577. <https://doi.org/10.1126/science.1063647>
- Wang R, Lorenzo-Martín F, Roth F (2006) PSGRN/PSCMP—A new code for calculating co-and post-seismic deformation, geoid and gravity changes based on the viscoelastic-gravitational dislocation theory. *Comput Geosci* 32(4):527–541. <https://doi.org/10.1016/j.cageo.2005.08.006>
- Wang Y, Wang M, Shen Z, Ge W, Wang K, Wang F, Sun J (2013) Inter-seismic deformation field of the Ganzi-Yushu fault before the 2010 mw 6.9 Yushu earthquake. *Tectonophysics* 584:138–143. <https://doi.org/10.1016/j.tecto.2012.03.026>
- Wang W, Qiao X, Yang S, Wang D (2017) Present-day velocity field and block kinematics of Tibetan plateau from GPS measurements. *Geophys J Int* 208(2):1088–1102. <https://doi.org/10.1093/gji/ggw445>
- Werner C, Wegmüller U, Strozzi T (2002) Processing strategies for phase unwrapping for InSAR applications. In proceedings of the European conference on synthetic aperture radar (EUSAR 2002) 1:353–356
- Wessel P, Smith WH, Scharroo R, Luis J, Wobbe F (2013) Generic mapping tools: improved version released. *Eos Trans Am Geophys Un* 94:409–410
- Wu Y, Jiang Z, Liang H, Pang Y, Zhu S, Chang L, Chen C, Li J (2018) Deformation response of Seismogenic faults to the Wenchuan MS 8.0 earthquake: a case study for the southern segment of the Longmenshan fault zone. *Remote Sens* 10: 894. <https://doi.org/10.3390/rs10060894>
- Xiong W, Qiao X, Liu G, Chen W, Nie Z (2018a) Coulomb stress evolution along the Kongur extensional system since 1895 and present seismic hazard. *Geodesy Geodyn* 10(1):1–9. <https://doi.org/10.1016/j.geog.2018.11.007>
- Xiong W, Yu C, Chen W, Nie Z, Tan K (2018b) Coulomb stress influence of 2010 Yushu earthquake on 2016 Zadou earthquake: earthquake and seismic hazard assessment on surrounding area. *J Geod Geodyn* 38:338–343. (In Chinese with English abstract). <https://doi.org/10.14075/j.jgg.2018.04.002>
- Xu W, Dutta R, Jónsson S (2015) Identifying active faults by improving earthquake locations with InSAR data and Bayesian estimation: the 2004 Tabuk (Saudi Arabia) earthquake sequence. *Bull Seismol Soc Am* 105(2A):765–775. <https://doi.org/10.1785/0120140289>
- Yin A, Kapp P, Murphy M, Manning C, Harrison T, Grove M, Ding L, Deng X, Wu C (1999) Significant late Neogene east-west extension in northern Tibet. *Geology* 27(9):787–790
- Yu J, Tan K, Zhang C, Zhao B, Wang D, Li Q (2019) Present-day crustal movement of the Chinese mainland based on global navigation satellite system data from 1998 to 2018. *Adv Space Res* 63:840–856. <https://doi.org/10.1016/j.asr.2018.10.001>
- Zhang P, Shen Z, Wang M, Gan W, Bürgmann R, Molnar P, Wang Q, Niu Z, Sun J, Wu J, Sun H, You X (2004) Continuous deformation of the Tibetan plateau from global positioning system data. *Geology* 32:809–812
- Zhao B, Bürgmann R, Wang D, Tan K, Du R, Zhang R (2017) Dominant controls of downdip afterslip and viscous relaxation on the postseismic displacements following the Mw 7.9 Gorkha, Nepal, earthquake. *J Geophys Res Solid Earth* 122: 8376–8401. <https://doi.org/10.1002/2017JB014366>
- Zhao B, Qi Y, Wang D, Yu J, Li Q, Zhang C (2018) Coseismic slip model of the 2018 M w 7.9 Gulf of Alaska earthquake and its seismic hazard implications. *Seismol Res Lett* 90: 642–648. <https://doi.org/10.1785/0220180141>

Publisher's note Springer Nature remains neutral with regard to jurisdictional claims in published maps and institutional affiliations.